28. Dark Energy

Revised August 2025 by D.H. Weinberg (Ohio State U.) and M. White (UC Berkeley; LBNL).

28.1 Repulsive Gravity and Cosmic Acceleration

In the first modern cosmological model, Einstein [1] modified his field equation of General Relativity (GR), introducing a "cosmological term" that enabled a solution with time-independent, spatially homogeneous matter density $\rho_{\rm m}$ and constant positive space curvature. Although Einstein did not frame it this way, one can view the "cosmological constant" Λ as representing a constant energy density of the vacuum [2], whose repulsive gravitational effect balances the attractive gravity of matter and thereby allows a static solution. After the development of dynamic cosmological models [3,4] and the discovery of cosmic expansion [5], the cosmological term appeared unnecessary, and Einstein and de Sitter [6] advocated adopting an expanding, homogeneous and isotropic, spatially flat, matter-dominated Universe as the default cosmology until observations dictated otherwise. Such a model has matter density equal to the critical density, $\Omega_{\rm m} \equiv \rho_{\rm m}/\rho_{\rm c} = 1$, and negligible contribution from other energy components [7].

By the mid-1990s, the Einstein-de Sitter model was showing numerous cracks, under the combined onslaught of data from the cosmic microwave background (CMB), large-scale galaxy clustering, and estimates of the matter density, the expansion rate (H_0), and the age of the Universe. As noted in a number of papers from this time, introducing a cosmological constant offered a potential resolution of many of these tensions, yielding the most empirically successful version of the inflationary cold dark matter scenario. In the late 1990s, supernova surveys by two independent teams provided direct evidence for accelerating cosmic expansion [8,9], establishing the cosmological constant model (with $\Omega_{\rm m} \simeq 0.3$, $\Omega_\Lambda \simeq 0.7$) as the preferred alternative to the $\Omega_{\rm m} = 1$ scenario. Shortly thereafter, CMB evidence for a spatially flat Universe [10,11], and thus for $\Omega_{\rm tot} \simeq 1$, cemented the case for cosmic acceleration by firmly eliminating the free-expansion alternative with $\Omega_{\rm m} \ll 1$ and $\Omega_\Lambda = 0$. Today, the accelerating Universe is well established by multiple lines of independent evidence from a tight web of precise cosmological measurements.

As discussed in the Big Bang Cosmology article of this *Review* (Sec. 22), the scale factor $R(t)$ of a homogeneous and isotropic Universe governed by GR grows at an accelerating rate if the pressure $p < -\frac{1}{3}\rho$ (in $c = 1$ units). A cosmological constant has $\rho_\Lambda =$ constant and pressure $p_\Lambda = -\rho_\Lambda$ (see Eq. 22.10), so it will drive acceleration if it dominates the total energy density. However, acceleration could arise from a more general form of "dark energy" that has negative pressure, typically specified in terms of the equation-of-state-parameter $w = p/\rho$ ($= -1$ for a cosmological constant). Furthermore, the conclusion that acceleration requires a new energy component beyond matter and radiation relies on the assumption that GR is the correct description of gravity on cosmological scales. The title of this article follows the common but inexact usage of "dark energy" as a catch-all term for the origin of cosmic acceleration, regardless of whether it arises from a new form of energy or a modification of GR. Our discussion in Secs. 28.2 and 28.3 draws on the extensive review of cosmic acceleration in Ref. [12], which provides further background explanation and references.

Below we will use the abbreviation ΛCDM to refer to a model with cold dark matter, a cosmological constant, inflationary initial conditions, standard radiation and neutrino content, and a flat Universe with $\Omega_{\rm tot} = 1$.

28.2 Theories of Cosmic Acceleration

28.2.1 *Dark Energy or Modified Gravity?*

A cosmological constant is the mathematically simplest, and perhaps the physically simplest, theoretical explanation for the accelerating Universe. The problem is explaining its unnaturally small magnitude, as discussed in Sec. 22.4.7 of this *Review*. An alternative (which still requires finding a way to make the cosmological constant zero or at least negligibly small) is that the accelerating cosmic expansion is driven by a new form of energy, such as a scalar field $\phi(\mathbf{x})$ with potential $V(\phi)$ [13]. The energy density and pressure of a canonical scalar field take the same forms as for inflationary scalar fields, given in Eq. (22.52) of the Big Bang Cosmology article. In the limit that $\frac{1}{2}\dot{\phi}^2 \ll |V(\phi)|$, the scalar field acts like a cosmological constant, with $p_\phi \simeq -\rho_\phi$. In this scenario, today's cosmic acceleration is closely akin to the epoch of inflation, but with radically different energy and timescale.

More generally, the value of $w = p_\phi/\rho_\phi$ in scalar field models evolves with time in a way that depends on $V(\phi)$ and on the initial conditions $(\phi_i, \dot{\phi}_i)$; some forms of $V(\phi)$ have attractor solutions in which the late-time behavior is insensitive to initial values. Many forms of time evolution are possible, including ones where w is approximately constant and broad classes where w "freezes" towards or "thaws" away from $w = -1$, with the transition occurring when the field comes to dominate the total energy budget. If ρ_ϕ is even approximately constant, then it becomes dynamically insignificant at high redshift, because the matter density scales as $\rho_{\rm m} \propto (1+z)^3$. "Early dark energy" models are ones in which ρ_ϕ is a small but not negligible fraction (*e.g.*, a few percent) of the total energy during the pre-recombination era, eventually evolving to become the dominant component at low redshift.

Instead of introducing a new energy component, one can attempt to modify gravity in a way that leads to accelerated expansion [14]. One option is to replace the Ricci scalar $\mathcal{R}$ with a function $\mathcal{R} + f(\mathcal{R})$ in the gravitational action [15]. Other changes can be more radical, such as introducing extra dimensions and allowing gravitons to "leak" off the brane that represents the observable Universe (the "DGP" model [16]). The DGP example has inspired a more general class of "galileon" and massive gravity models. Constructing viable modified gravity models is challenging, in part because it is easy to introduce theoretical inconsistencies (such as "ghost" fields with negative kinetic energy), but above all because GR is a theory with many high-precision empirical successes on solar system scales [17]. Modified gravity models typically invoke screening mechanisms that force model predictions to approach those of GR in regions of high density or strong gravitational potential. Screening offers potentially distinctive signatures, since the strength of gravity (*i.e.*, the effective value of $G_{\rm N}$) can vary by order unity in environments with different gravitational potentials.

More generally, one can search for signatures of modified gravity by comparing the history of cosmic structure growth to the history of cosmic expansion. Within GR, these two are linked by a consistency relation, as described below (Eq. (28.2)). Modifying gravity can change the predicted rate of structure growth, and it can make the growth rate dependent on scale or environment. In some circumstances, modifying gravity alters the combinations of potentials responsible for gravitational lensing and the dynamics of non-relativistic tracers (such as galaxies or stars) in different ways (see Sec. 22.4.7 in this *Review*), leading to order unity mismatches between the masses of objects inferred from lensing and those inferred from dynamics in unscreened environments.

At present there are no fully realized and empirically viable modified gravity theories that explain the observed level of cosmic acceleration. The constraints on $f(\mathcal{R})$ models now force them so close to GR that they cannot produce acceleration without introducing a separate dark energy component [18]. The DGP model is empirically ruled out by several tests, including the expansion

history, the integrated Sachs-Wolfe effect, and redshift-space distortion measurements of the structure growth rate [19]. The near-simultaneous arrival of gravitational waves and electromagnetic signals from the neutron star merger event GW170817, which shows that gravitational waves travel at almost exactly the speed of light, is a further strong constraint on modified gravity theories [20]. The elimination of models should be considered an important success of the program to empirically test theories of cosmic acceleration. However, it is worth recalling that there was no fully realized gravitational explanation for the precession of Mercury's orbit prior to the completion of GR in 1915, and the fact that no complete and viable modified gravity theory exists today does not mean that one will not arise in the future. In the meantime, we can continue empirical investigations that can tighten restrictions on such theories or perhaps point towards the gravitational sector as the origin of accelerating expansion.

28.2.2 *Expansion History and Growth of Structure*

The main line of empirical attack on dark energy is to measure the history of cosmic expansion and the history of matter clustering with the greatest achievable precision over a wide range of redshift. Within GR, the expansion rate $H(z)$ is governed by the Friedmann equation (see the articles on Big Bang Cosmology and Cosmological Parameters—Secs. 22 and 25 in this *Review*). For dark energy with an equation of state $w(z)$, the cosmological constant contribution to the expansion, Ω_Λ, is replaced by a redshift-dependent contribution. The evolution of the dark energy density follows from Eq. (22.10),

$$\Omega_{\rm de}\frac{\rho_{\rm de}(z)}{\rho_{\rm de}(z=0)} = \Omega_{\rm de}\exp\left[3\int_0^z [1+w(z')]\frac{dz'}{1+z'}\right] \;=\; \Omega_{\rm de}(1+z)^{3(1+w)}, \tag{28.1}$$

where the second equality holds for constant w. If $\Omega_{\rm m}$, $\Omega_{\rm r}$, and the present value of $\Omega_{\rm tot}$ are known, then measuring $H(z)$ pins down $w(z)$. (Note that $\Omega_{\rm de}$ is the same quantity denoted $\Omega_{\rm v}$ in Sec. 22, but we have adopted the 'de' subscript to avoid implying that dark energy is necessarily a vacuum effect.) The evolution of $\rho_{\rm de}$ can be more complicated than Eq. (28.1) in scenarios with non-gravitational coupling between dark energy and other components, *e.g.*, "decay" into dark matter or radiation.

While some observations can probe $H(z)$ directly, others measure the distance-redshift relation. The basic relations between angular diameter distance or luminosity distance and $H(z)$ are given in Ch. 22 —and these are generally unaltered in time-dependent dark energy or modified gravity models. We will often refer to the comoving angular diameter distance, $D_{\rm M}(z) = (1+z)D_{\rm A}(z)$, which relates comoving transverse size to angular size. The subscript M is conventional notation because this distance is also the one that relates transverse velocity to proper motion.

In GR-based linear perturbation theory, the density contrast $\delta(\mathbf{x},t) \equiv \rho(\mathbf{x},t)/\bar\rho(t) - 1$ of pressureless matter grows in proportion to the linear growth function $G(t)$ (not to be confused with the gravitational constant $G_{\rm N}$), which follows the differential equation

$$\ddot G + 2H(z)\dot G - \frac{3}{2}\Omega_{\rm m}H_0^2(1+z)^3 G = 0\ . \tag{28.2}$$

To a good approximation, the logarithmic derivative of $G(z)$ is

$$f(z) \equiv -\frac{d\ln G}{d\ln(1+z)} \simeq \left[\Omega_{\rm m}(1+z)^3\frac{H_0^2}{H^2(z)}\right]^\gamma\ , \tag{28.3}$$

where $\gamma \simeq 0.55$ for relevant values of cosmological parameters [21]. In an $\Omega_{\rm m} = 1$ Universe, $G(z) \propto (1+z)^{-1}$, but growth slows when $\Omega_{\rm m}$ drops significantly below unity. One can integrate

Eq. (28.3) to get an approximate integral relation between $G(z)$ and $H(z)$, but the full (numerical) solution to Eq. (28.2) should be used for precision calculations. Even in the non-linear regime, the amplitude of clustering is determined mainly by $G(z)$, so observations of non-linear structure can be used to infer the linear $G(z)$, provided one has good theoretical modeling to relate the two.

In modified gravity models the growth rate of gravitational clustering may differ from the GR prediction. A general strategy to test modified gravity, therefore, is to measure both the expansion history and the growth history to see whether they yield consistent results for $H(z)$ or $w(z)$.

28.2.3 *Parameters*

Constraining a general history of $w(z)$ is nearly impossible, because the dark energy density, which affects $H(z)$, is given by an integral over $w(z)$, and distances and the growth factor involve a further integration over functions of $H(z)$. Oscillations in $w(z)$ over a range $\Delta z/(1+z) \ll 1$ are therefore extremely difficult to constrain. It has become conventional to phrase constraints or projected constraints on $w(z)$ in terms of a linear evolution model,

$$w(a) = w_0 + w_a(1-a) = w_p + w_a(a_p - a), \tag{28.4}$$

where $a \equiv (1+z)^{-1}$, w_0 is the value of w at $z = 0$, and w_p is the value of w at a "pivot" redshift $z_p \equiv a_p^{-1} - 1$, where it is best constrained by a given set of experiments. For typical data combinations, $z_p \simeq 0.5$. This simple parameterization can provide a good approximation to the predictions of many physically motivated models for observables measured with percent-level precision. A widely used "Figure of Merit" (FoM) for dark energy experiments [22] is the projected combination of errors $[\sigma(w_p)\sigma(w_a)]^{-1}$. Ambitious experiments with 0.1–0.3% precision on observables can constrain richer descriptions of $w(z)$, which can be characterized, *e.g.*, by principal components.

There has been less convergence on a standard parameterization for describing modified gravity theories. Deviations from the GR-predicted growth rate can be described by a deviation $\Delta\gamma$ in the index of Eq. (28.3), together with an overall multiplicative offset relative to the $G(z)$ expected from extrapolating the CMB-measured fluctuation amplitude to low redshift. However, these two parameters may not accurately capture the growth predictions of all physically interesting models. Another important parameter to constrain is the ratio of the gravitational potentials governing space curvature and the acceleration of non-relativistic test particles. The possible phenomenology of modified gravity models is rich [23], which enables many consistency tests but complicates the task of constructing parameterized descriptions.

The more general set of cosmological parameters is discussed elsewhere in this *Review* (Sec. 25), but here we highlight a few that are particularly important to the dark energy discussion.

- The dimensionless Hubble parameter $h \equiv H_0/100\ \mathrm{km\,s^{-1}\,Mpc^{-1}}$ determines the present day value of the critical density and the overall scaling of distances inferred from redshifts.
- Ω_m and Ω_{tot} affect the expansion history and the distance-redshift relation.
- The sound horizon $r_s = \int_0^{t_{rec}} c_s(t)dt/a(t)$, the comoving distance that pressure waves can propagate between $t = 0$ and recombination, determines the physical scale of the acoustic peaks in the CMB and the baryon acoustic oscillation (BAO) feature in low-redshift matter clustering [24].
- The amplitude of matter fluctuations, conventionally represented by the quantity $\sigma_8(z)$, scales the overall amplitude of growth measures such as weak lensing or redshift-space distortions (discussed in the next section).

Specifically, $\sigma_8(z)$ refers to the rms fluctuation of the matter overdensity $\rho/\bar{\rho}$ in spheres of radius $8\,h^{-1}$Mpc, computed from the linear theory matter power spectrum at redshift z, and σ_8 on its

own refers to the value at $z = 0$ (just like our convention for $\Omega_{\rm m}$).

While discussions of dark energy are frequently phrased in terms of values and errors on quantities like $w_{\rm p}$, $w_{\rm a}$, $\Delta\gamma$, and $\Omega_{\rm tot}$, parameter precision is the means to an end, not an end in itself. The underlying goal of empirical studies of cosmic acceleration is to address two physically profound questions:

- 1. Does acceleration arise from a breakdown of GR on cosmological scales or from a new energy component that exerts repulsive gravity within GR?
- 2. If acceleration is caused by a new energy component, is its energy density constant in space and time, as expected for a fundamental vacuum energy, or does it show variations that indicate a dynamical field?

Substantial progress towards answering these questions, in particular any definitive rejection of the cosmological constant "null hypothesis," would be a major breakthrough in cosmology and fundamental physics.

28.3 Observational Probes

We briefly summarize the observational probes that play the greatest role in current constraints on dark energy. Further discussion can be found in other articles of this *Review*, in particular Secs. 25 (Cosmological Parameters) and 29 (The Cosmic Microwave Background), and in Ref. [12], which provides extensive references to background literature. Recent observational results from these methods are discussed in Sec. 28.4.

28.3.1 *Methods, Sensitivity, Systematics*

Cosmic Microwave Background Anisotropies: Although CMB anisotropies provide limited information about dark energy on their own, CMB constraints on the geometry, matter content, and radiation content of the Universe play a critical role in dark energy studies when combined with low-redshift probes. In particular, CMB data supply measurements of $\theta_{\rm s} = r_{\rm s}/D_{\rm M}(z_{\rm rec})$, the angular size of the sound horizon at recombination, from the angular location of the acoustic peaks, measurements of $\Omega_{\rm m}h^2$ and $\Omega_{\rm b}h^2$ from the heights of the peaks, and normalization of the amplitude of matter fluctuations at $z_{\rm rec}$ from the amplitude of the CMB fluctuations themselves. The comparison of the acoustic scale to the diffusion damping scale helps to constrain the expansion rate near recombination. *Planck* data yield a 0.18% determination of $r_{\rm s}$, which scales as $(\Omega_{\rm m}h^2)^{-0.25}$ for cosmologies with standard matter and radiation content. The uncertainty in the matter fluctuation amplitude at the epoch of recombination is 0.5%. Secondary anisotropies, including the integrated Sachs-Wolfe effect, the Sunyaev-Zeldovich (SZ, [25]) effect, and weak lensing of primary anisotropies, provide additional information about dark energy by constraining low-redshift structure growth.

Type Ia Supernovae (SN): Type Ia supernovae, produced by the thermonuclear explosions of white dwarfs, exhibit 10–15% scatter in peak luminosity after correction for light-curve duration (the time to rise and fall) and color (which is a diagnostic of dust extinction). Since the peak luminosity is not known *a priori*, supernova surveys constrain ratios of luminosity distances $D_{\rm L}(z)$ at different redshifts. If one is comparing a high-redshift sample to a local calibrator sample measured with much higher precision (and distances inferred from Hubble's law), then one essentially measures the luminosity distance in h^{-1}Mpc, constraining the combination $hD_{\rm L}(z)$. With distance uncertainties of 5–8% per well observed supernova, a sample of around 100 SNe is sufficient to achieve sub-percent statistical precision. The percent-level systematic uncertainties in current samples are dominated by uncertainties associated with photometric calibration, dust extinction corrections, and modeling the correlations among supernova luminosity, color, light-curve shape, and host galaxy properties. Another potential systematic is redshift evolution of the supernova population itself, which can be

tested by analyzing subsamples grouped by spectral properties or host galaxy properties to confirm that they yield consistent results. Recent analyses of large supernova compilations calibrate these systematic uncertainties internally in parallel with cosmological constraints, with an overall error budget that has similar contributions from systematic and statistical uncertainties (*e.g.*, [26]).

Baryon Acoustic Oscillations (BAO): Pressure waves that propagate in the pre-recombination photon-baryon fluid imprint a characteristic scale in the clustering of matter and galaxies, which appears in the galaxy correlation function as a localized peak at the sound horizon scale $r_{\rm s}$, or in the power spectrum as a series of oscillations. Since observed galaxy coordinates consist of angles and redshifts, measuring this "standard ruler" scale in a galaxy redshift survey determines the angular diameter distance $D_{\rm A}(z)$ and the expansion rate $H(z)$, which convert coordinate separations to comoving distances. Errors on the two quantities are correlated, and in existing galaxy surveys the best determined combination is approximately $D_{\rm V}(z) = [czD_{\rm M}^2(z)/H(z)]^{1/3}$. As a useful rule of thumb, a survey that densely maps structure at redshift z over a comoving volume V, and is therefore limited by sample variance rather than shot noise, measures $D_{\rm M}(z)$ with a fractional error of $0.005(V/10\,{\rm Gpc}^3)^{-1/2}$ and $H(z)$ with a fractional error 1.6–1.8 times higher. Large galaxy and quasar redshift surveys now provide precise BAO measurements out to $z \simeq 1.5$. At redshifts $z > 2$, BAO can also be measured in the Lyman-α forest of intergalactic hydrogen absorption towards background quasars, where the fluctuating absorption pattern provides tens or hundreds of samples of the density field along each quasar sightline. For Lyman-α forest BAO, the best measured parameter combination is more heavily weighted towards $H(z)$ because of strong redshift-space distortions, which enhance clustering in the line-of-sight direction. Cross-correlation between the Lyman-α forest and quasars sharpens the constraints on $D_{\rm M}(z)$. Photometric redshifts in optical imaging surveys can be used to measure BAO in the angular direction, though the typical distance precision is a factor of 3–4 lower compared to a well sampled spectroscopic survey of the same area, and angular BAO measurements do not directly constrain $H(z)$. BAO distance measurements complement SN distance measurements by providing absolute rather than relative distances (with precise calibration of $r_{\rm s}$ from the CMB) and by having greater achievable precision at high redshift thanks to the increasing comoving volume available. Theoretical modeling suggests that BAO measurements from even the largest feasible redshift surveys will be limited by statistical rather than systematic uncertainties [27].

Weak Gravitational Lensing: Gravitational light bending by a clustered distribution of matter shears the shapes of higher redshift background galaxies in a spatially coherent manner, producing a correlated pattern of apparent ellipticities. By studying the weak lensing signal for source galaxies binned by photometric redshift (estimated from broad-band colors), one can probe the history of structure growth. "Cosmic shear" weak lensing uses the correlation of source ellipticities to deduce the clustering of intervening matter. "Galaxy-galaxy lensing" (GGL) uses the correlation between a shear map and a foreground galaxy sample to measure the galaxy-mass cross-correlation function, which can be combined with galaxy clustering to constrain total matter clustering. For a specified expansion history, the predicted signals scale approximately as $\sigma_8\Omega_{\rm m}^{\alpha}$, with $\alpha = 0.3$–0.5. The predicted signals also depend on the distance-redshift relation, so weak lensing becomes a sharper probe of matter clustering when combined with SN or BAO measurements that pin down $D_{\rm M}(z)$. Conversely, with CMB lensing and redshift space distortions now giving competitive constraints on matter clustering (see below), weak lensing is becoming a valuable test of the expansion history.

The most challenging systematics in weak lensing are shape measurement biases, biases in the distribution of photometric redshifts, and intrinsic alignments of galaxy orientations that could contaminate the lensing-induced signal. Weak lensing of CMB anisotropies is an increasingly powerful tool, in part because it circumvents many of these observational and astrophysical systematics. Predicting the large-scale weak lensing signal is straightforward in principle, but the number of

independent modes on large scales is small, and the inferences are therefore dominated by sample variance. Exploiting small-scale measurements, for tighter constraints, requires modeling the effects of complex physical processes such as star formation and feedback on the matter power spectrum. Strong gravitational lensing can also provide constraints on dark energy, either through time-delay measurements that probe the absolute distance scale, or through measurements of multiple-redshift lenses that constrain distance ratios. The primary uncertainty for strong lensing constraints is modeling the mass distribution of the lens systems.

Clusters of Galaxies: Like weak lensing, the abundance of massive dark-matter halos probes structure growth by constraining $\sigma_8\Omega_{\rm m}^{\alpha}$, where $\alpha \simeq 0.3$–0.5. These halos can be identified as dense concentrations of galaxies or through the signatures of hot (10^7–$10^8\,$K) gas in X-ray emission or SZ distortion of the CMB. The critical challenge in cluster cosmology is calibrating the relation between the halo mass as predicted from theory and the observable mass proxy used for cluster identification, with percent-level accuracy needed for clusters to remain competitive with other growth probes. The most promising approach uses stacked weak lensing to measure projected cluster-mass cross-correlations, making cluster cosmology analogous to GGL but with clusters rather than galaxies chosen as reference points. Sample selection effects and the influence of baryonic physics on halo mass profiles remain serious challenges for cluster cosmology.

Redshift-Space Distortions (RSD) and the Alcock-Paczynski (AP) Effect: Redshift-space distortions of galaxy clustering, induced by peculiar motions, probe structure growth by constraining the parameter combination $f(z)\sigma_8(z)$, where $f(z)$ is the growth rate defined by Eq. (28.3). The most secure constraints come from large scales (comoving separations $r \gtrsim 10\,h^{-1}$Mpc or wavenumbers $k \lesssim 0.2h\,{\rm Mpc}^{-1}$), which are adequately described by perturbation theory. Taking advantage of the higher measurement precision on smaller scales requires accurate models of non-linear gravitational evolution and the non-linear bias between galaxy and matter distributions. A second source of anisotropy arises if one adopts the wrong cosmological metric to convert angles and redshifts into comoving separations, a phenomenon known as the Alcock-Paczynski effect [28]. Demanding isotropy of clustering at redshift z constrains the parameter combination $H(z)D_{\rm M}(z)$. The main challenge for the AP method is correcting for the anisotropy induced by peculiar velocity RSD.

Low Redshift Measurement of H_0: The value of H_0 sets the current value of the critical density $\rho_{\rm c} = 3H_0^2/8\pi G_{\rm N}$, and combination with CMB measurements provides a long lever arm for constraining the evolution of dark energy. The challenge in conventional H_0 measurements is establishing distances to galaxies that are "in the Hubble flow," *i.e.*, far enough away that their peculiar velocities are small compared to the expansion velocity $v = H_0 d$. This can be done by building a ladder of distance indicators tied to stellar parallax on its lowest rung, or by using gravitational-lens time delays or geometrical measurements of maser data to circumvent this ladder.

28.3.2 *Dark Energy Experiments*

Most observational applications of the above methods now take place in the context of large cosmological surveys, for which constraining dark energy and modified gravity theories is a central objective. We are now at an exciting phase in which most of the "Stage III" experiments (in the parlance of Ref. [29]) have completed observations and in some cases final analysis, and the more powerful "Stage IV" experiments are underway or beginning operations in the near future.

Beginning with the main Stage III imaging surveys, all designed with weak lensing as a primary goal, the Kilo Degree Survey (KiDS) imaged 1350 deg^2, the Dark Energy Survey (DES) imaged 5000 deg^2, and the Subaru Hyper-Suprime Camera (HSC) imaged about 1200 deg^2. The statistical power and systematics control of a weak lensing survey depend on area, depth, and image quality, and on filter coverage and spectroscopic calibration for photometric redshifts. All three surveys have contributed to the current understanding of matter clustering evolution and its implications

for dark energy. Recent cosmological analyses from these survey teams include Refs. [30] (KiDS, based on the final data set), [31] (DES, based on the 3-year data set), and [32] (HSC, based on the 3-year data set).

Supernova cosmology has advanced largely through unified analyses of compilation data sets obtained from multiple telescopes, with Pantheon+ [33] and Union3 [34] being two state-of-the-art compilations. The largest single-telescope supernova survey comes from DES, and its final sample includes about 1500 SNe Ia observed by DES with $0.1 < z < 1.1$ and 194 local SNe Ia observed by a variety of telescopes [35]. Although these three analyses have many supernovae in common, different calibration and modeling choices can lead to significant differences in their cosmological implications, as discussed in Section 28.4. The local sample plays an important role in calibrating the supernova luminosity scale, and matching these local supernovae to their higher redshift counterparts has emerged as an important challenge.

The Stage III Baryon Oscillation Spectroscopic Survey (BOSS) and its successor eBOSS used fiber-fed optical spectrographs to map the redshift-space distributions of about two million galaxies and quasars and Lyman-α forest spectra of about 200,000 high-redshift quasars. These 3-dimensional maps enabled BAO and RSD measurements over the redshift range $0.1 < z < 2.5$, including percent-level determinations of $D_{\rm M}(z)$ and $H(z)$ at multiple redshifts [36]. The combination of CMB and BAO measurements has allowed strong constraints on dark energy and cosmological parameters from probes that have relatively simple physics, mostly described by linear perturbation theory.

Stage IV experiments seek a roughly order-of-magnitude gain in data volume relative to Stage III experiments, as well as the improvements in data quality and systematics control needed to exploit their greater statistical power. First out of the gate is the Dark Energy Spectroscopic Instrument (DESI), which follows a strategy similar to BOSS/eBOSS but on a much grander scale, using a larger telescope (4-m versus 2.5-m) and a much higher fiber multiplex (5000 versus 1000). DESI began full operations in May 2021, and its three-year data set includes over 30 million galaxies and quasars and 0.8-million Lyman-α forest spectra [37]. The BAO measurements from this data set play a central role in our discussion of current dark energy constraints below.

The *Euclid* space mission, launched in July 2023, will image 14,000 deg^2 through a wide optical filter for measurements of weak lensing and photometric galaxy clustering, and it will conduct a slitless spectroscopic survey over the same area at NIR wavelengths to enable BAO and RSD measurements at $0.9 < z < 2$. *Euclid* presented early science results in mid-2024 (*e.g.*, [38]), and the consortium is now working towards its first cosmological results. Vera Rubin Observatory will obtain deep multi-band optical imaging of about 18,000 deg^2 for weak lensing and photometric galaxy clustering, with high-cadence time-domain monitoring of smaller fields to identify and measure light curves for many thousands of Type Ia supernovae. First-light images from Rubin were presented in summer 2025, and the decade-long Legacy Survey of Space and Time (LSST, [39]) will begin regular operations in autumn 2025.

The *Nancy Grace Roman Space Telescope*, scheduled for launch in October 2026, will devote 1.4 years of its 5-year prime mission to a high-latitude, wide area survey, covering 2400 deg^2 in three NIR imaging bands and slitless spectroscopy (galaxy redshifts $0.7 < z < 3$), plus an additional 2700 deg^2 of single filter imaging. A further 0.5 years of observing time will be devoted to a time-domain survey expected to measure light curves for more than 10,000 supernovae extending to $z > 2$. Both surveys are described in Ref. [40]. DESI, *Euclid*, Rubin, and *Roman* each have distinctive strengths as cosmological survey experiments, and the history of Stage III analyses suggests that comparisons and cross-calibrations among them will play a crucial role in extracting their cosmological lessons.

The next generation of CMB experiments, in particular the Simons Observatory and Advanced Simons Observatory, will provide tighter constraints on cosmological parameters from primary

anisotropies *and* much higher precision CMB lensing maps. These maps will be powerful probes of matter clustering evolution on their own and in concert with galaxy surveys.

28.4 Current Constraints on Expansion, Growth, and Dark Energy

The last decade has seen dramatic progress in measurements of the cosmic expansion history and structure growth, leading to much tighter constraints on the parameters of dark energy models. Much of this progress has come from the intermediate or final results of the Stage III dark energy experiments described in the preceding Section, along with early results from DESI. Exquisitely precise maps of CMB temperature and polarization anisotropies, from *WMAP* and *Planck* and higher resolution ground-based experiments, provide tight constraints on the matter and baryon density and the distance to the last-scattering surface, as well as sharp limits on non-standard energy components in the pre-recombination Universe (see Section 29). CMB lensing maps provide increasingly powerful measurements of low redshift matter clustering, on their own and through cross-correlation with galaxy and cluster distributions. Cepheid-based distance-ladder measurements of H_0 have reached statistical precision of around 1%, though independent analyses using different distance indicators vary at the few percent level. For all of these experiments, the high statistical precision of current measurements demands stringent control of systematic uncertainties, and much of the community's effort has gone into assessing and mitigating systematics using both empirical and theoretical methods.

As a pedagogical illustration of current measurements of the cosmic expansion history, Figure 28.1 compares distance-redshift measurements from DESI BAO data and DES SN data to the predictions for a flat Universe with a cosmological constant. Transverse BAO measurements determine the comoving angular diameter distance $D_{\rm M}(z)$, and line-of-sight BAO measurements determine the expansion rate $H(z) = c/D_{\rm H}(z)$, and thus the local slope of the distance-redshift relation. DESI uses a variety of galaxy and quasar tracers to measure BAO distances in multiple redshift bins from $z = 0.3$ to $z = 1.5$, and the Lyman-α forest to provide measurements in a seventh bin at $z = 2.3$. After standardizing the peak SN luminosity using light-curve shape and color, SN data determine $D_{\rm M}(z)$ from the apparent flux. For visualization, the roughly 1700 SNe of the DES sample have here been averaged into seven redshift bins from $z = 0.005$ to $z = 0.9$. At the level that is visually discernible on this plot, the BAO and SN measurements show excellent agreement with each other and with the predictions of a flat ΛCDM model, given parameter values determined independently from *Planck* CMB data.

28.4.1 *Evolving dark energy?*

In detail, the CMB, BAO, and SN data sets can each be fit well individually by a ΛCDM model, but the preferred parameter values (specifically H_0 and $\Omega_{\rm m} = 1 - \Omega_\Lambda$) are different. This tension of parameter values could be a sign that the underlying model is incorrect. Within ΛCDM, the DESI Collaboration reports a tension of about 2σ between BAO and CMB alone, with the exact value depending on the details of the CMB data set. They find that allowing non-zero curvature or a constant $w \neq -1$ does little to alleviate the tension between the CMB and BAO data, and they instead focus on $\mathtt{w_0w_a CDM}$, a flat Universe with cold dark matter and a dark energy equation-of-state described by Eq. (28.4). Figure 28.2 shows their 68% and 95% constraints in the $w_0 - w_{\rm a}$ plane inferred from DESI+*Planck* alone (pink dashed contour) or from DESI+*Planck* combined with SN data from the DES, Union3, or Pantheon+ compilations (filled contours, as labeled). In all cases, the ΛCDM values ($w_0 = -1$, $w_{\rm a} = 0$) lie outside the 95% contour, but the significance of the discrepancy depends on the chosen data combination. For DESI+CMB, Ref. [37] finds a $\Delta\chi^2_{\rm MAP} = -12.5$ between the most probable $\mathtt{w_0w_a CDM}$ model and the most probable ΛCDM model. Accounting for the two extra parameters of $\mathtt{w_0w_a CDM}$, this difference corresponds to a frequentist significance of 3.1σ assuming Gaussian error distributions. Adding DES SN raises the significance

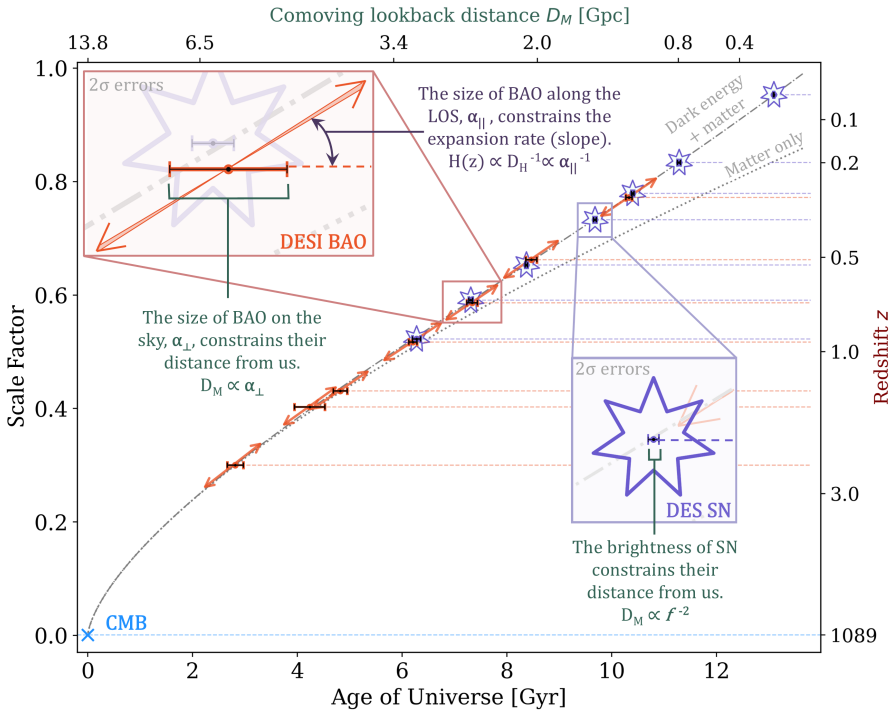

Figure 28.1: Expansion history of the Universe as measured by BAO and Type Ia SNe, adapted (by C. Lamman) from Ref. [37]. Black points with horizontal 2σ error bars show transverse BAO measurements from DESI galaxy or Lyman-α forest samples at different redshifts (right axis), plotted against the inferred comoving angular diameter distance $D_{\rm M}$ (top axis). Orange arrows show the expansion rate — the slope of the age-distance relation — inferred at these redshifts from the line-of-sight BAO measurements. Blue stars surrounding blue horizontal error bars show binned measurements of $D_{\rm M}$ from DES SNe; these measurements of relative distance have been normalized to match the absolute scale of the BAO. The dashed curve shows the predicted distance-redshift relation of a flat ΛCDM model with $\Omega_{\rm m} = 0.315$ and $h = 0.674$, the best-fit parameters inferred from *Planck* CMB data [41]. The dotted curve shows the prediction of a flat model with $\Omega_{\rm m} = 1$ and $h = 0.674$. The age of the Universe on the bottom axis corresponds to the ΛCDM model and would be slightly different for the $\Omega_{\rm m} = 1$ model. Predictions for an open universe with $\Omega_\Lambda = 0$ would be intermediate between the two models plotted, but still strongly inconsistent with the BAO and SN data and also with the angular scale of CMB anisotropies.

to 4.2σ, but using the Pantheon+ SNe instead of DES reduces the significance to 2.8σ.

Figure 28.3 shows the features of the data that lead to these model constraints, with all distances divided by the predictions of the fiducial *Planck* ΛCDM model so that the percent-level error bars can be clearly discerned. Several of the DESI data points in the upper panels, especially the $D_{\rm H}$ points at $z = 0.5$ and $z = 0.7$, lie outside the 1σ band of *Planck*-based ΛCDM predictions. While a joint fit (purple curve) comes closer to the DESI points, as expected, this compromise ΛCDM model does not give good agreement with either *Planck* or DESI. The red-dashed curve shows a `w0waCDM` model with $w_0 = -0.752$ and $w_{\rm a} = -0.86$, the best-fit values from the DESI+*Planck*+DES SN combination. This model gives noticeably better agreement with the DESI data and (while it

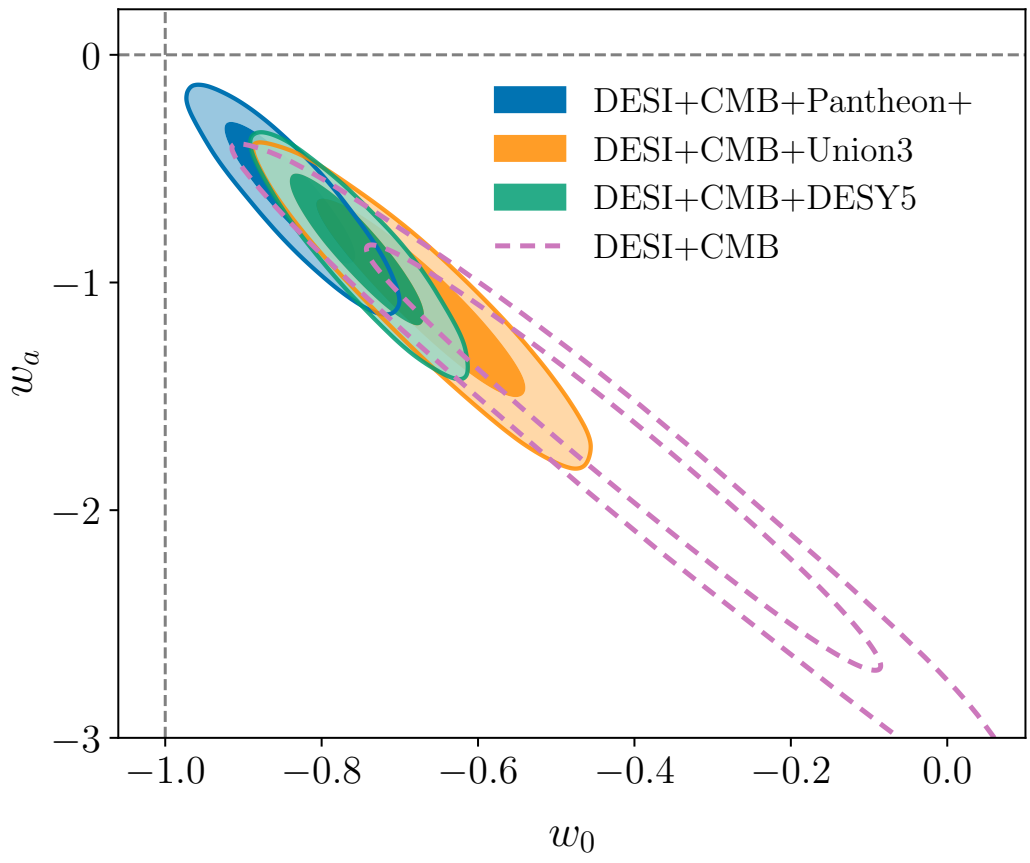

Figure 28.2: Constraints on parameters of the $\mathtt{w_0w_aCDM}$ dark energy model from combinations of CMB, BAO, and supernova (SN) data, taken from Ref. [37]. Dashed contours show 68% and 95% confidence intervals on w_0 and w_a inferred from DESI DR2 BAO measurements and *Planck* 2018 CMB anisotropy data. Filled contours show the impact of adding SN data from the DES Y5 compilation (green), the Pantheon+ compilation (blue), or the Union3 compilation (orange). Dashed gray lines mark the ΛCDM values of $w_0 = -1$, $w_\mathrm{a} = 0$.

cannot be seen from this plot) with the CMB data. The DES SN data (lower left panel) show a sharp preference for this $\mathtt{w_0w_aCDM}$ model over the DESI+CMB ΛCDM model, with the critical distinction being a 2% difference in the local distance scale measured by the $z = 0.005$ SNe relative to those at $z = 0.3$-0.7. However, the Pantheon+ SN measurements (lower right panel) are equally consistent with the $\mathtt{w_0w_aCDM}$ and ΛCDM models, with the key difference from DES being the $z = 0.005$ data point.

Figure 28.4 shows the evolution of the dark energy density ρ_de predicted by the $\mathtt{w_0w_aCDM}$ model compared to the constant ρ_de of ΛCDM. In the $\mathtt{w_0w_aCDM}$ model, $\rho_\mathrm{de}/\rho_\mathrm{de,0}$ climbs to a maximum of about 1.1 at $z \simeq 0.5$, then falls back to 1.0 at $z \simeq 1$ and declines slowly towards zero at higher redshift. The bump in the total energy density ($\rho_\mathrm{tot} = \rho_\mathrm{de} + \rho_\mathrm{m}$) produces a minimum in $D_\mathrm{H}(z) \propto \rho_\mathrm{tot}^{-1/2}$ and a smoother minimum in $D_\mathrm{M}(z)$, as seen in the red-dashed curves of Figure 28.3. The decline in ρ_de at high redshift is required so that the model reproduces the precisely measured angular scale of CMB anisotropies, which depends on the ratio $r_\mathrm{s}/D_\mathrm{M}(z_\mathrm{rec})$.

This preferred model is physically surprising in at least two respects. First, the value of w_a implies rapid evolution of the equation of state, with an order-unity change of w over a $\Delta z \sim 1$

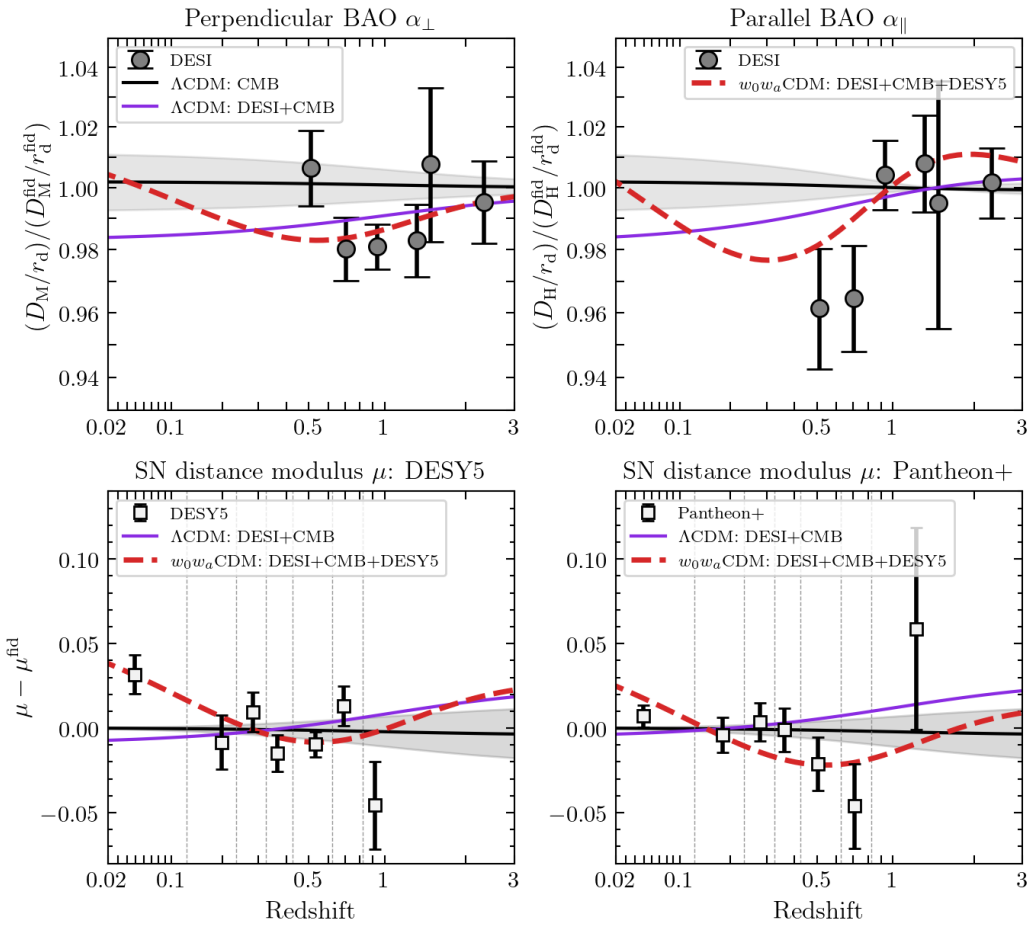

Figure 28.3: Distance-redshift measurements ("Hubble diagram") from BAO and SN, scaled by predictions of the fiducial *Planck* ΛCDM model to highlight subtle deviations, adapted (by Q. Li) from Ref. [37]. Upper panels show BAO measurements transverse (left) and parallel (right) to the line of sight, with gray circles representing the DESI DR2 measurements. Lower panels show binned measurements of the distance modulus (squares) inferred from DES Y5 (left) or Pantheon+ (right). In all panels, the gray band shows the $\pm1\sigma$ range of the *Planck* predictions assuming ΛCDM, and purple curves show predictions of the ΛCDM model that is the best joint fit to the DESI BAO and *Planck* CMB measurements. Red dashed curves show predictions of a $\mathtt{w_0w_aCDM}$ model with $w_0 = -0.752$, $w_a = -0.86$, the best-fit parameters for the DESI+CMB+DESY5 combination. Because the fiducial SN absolute magnitude is not known *a priori*, data points in the lower panels are free to move up or down by a constant shift in μ; here they have been normalized to give an error-weighted mean of $\mu - \mu_{fid} = 0$, and each model curve is pinned to the average of the SN data. The lowest redshift DES data point disagrees by 0.04 mag (2% in distance) with the prediction of the DESI+CMB ΛCDM model.

redshift interval. Second, w evolves from $w < -1$ at high redshift to $w > -1$ at low redshift, a "phantom crossing" behavior that cannot arise in dark energy models with a single scalar field [42]. This unusual behavior is not just an artifact of the $w_0 - w_a$ parameterization, as analyses of the DESI data with more flexible $w(z)$ models still show a significant preference for phantom crossing, and models that are forced to maintain $w \geq -1$ fit the data less well.

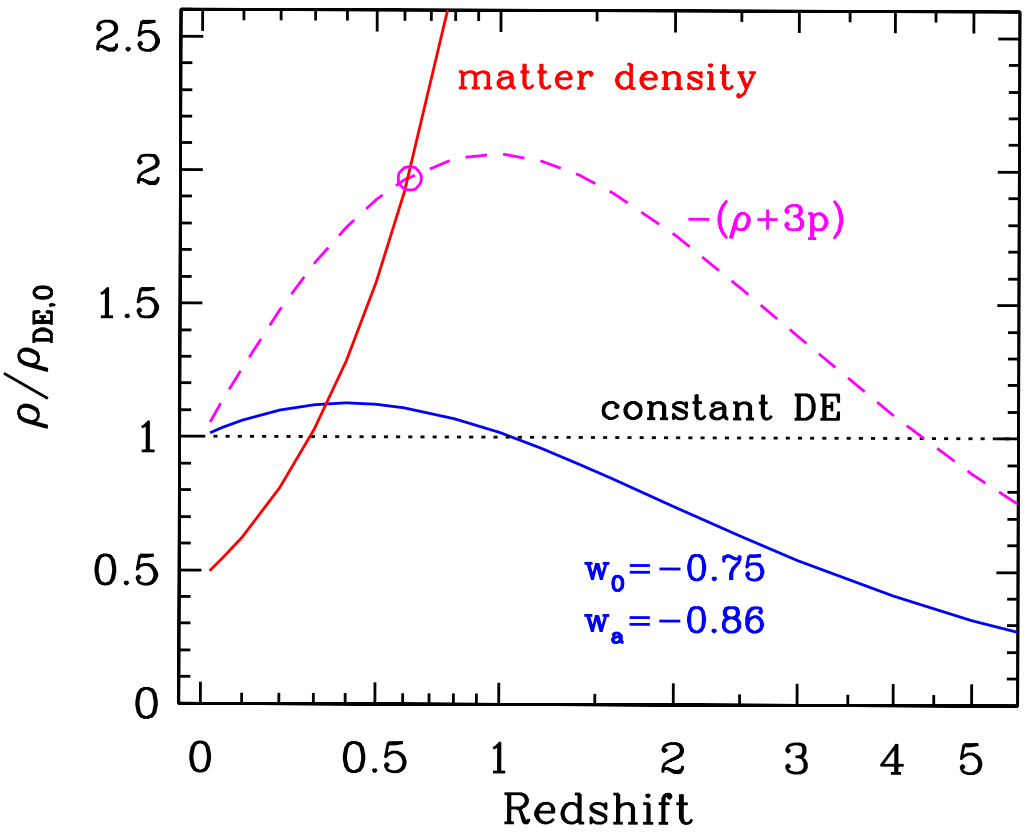

Figure 28.4: Evolution of dark energy in a model with $w_0 = -0.75$, $w_\mathrm{a} = -0.86$, the best-fit values from DESI+CMB+DES SN (red-dashed curve of Figure 28.3). The blue solid curve shows the evolution of the dark energy density $\rho_\mathrm{de}(z)$, while the pink dashed curve shows the combination $-(\rho + 3p)$ that enters the acceleration equation. Cosmic acceleration begins when this curve goes above the matter density (red solid curve), which follows $\rho_\mathrm{m} \propto (1+z)^3$; this intersection occurs at $z \simeq 0.62$ (pink circle). The dashed horizontal line shows the constant ρ_de of the ΛCDM model, which has $-(\rho + 3p)/\rho_\mathrm{de,0} = 2$ at all times. The redshift axis is scaled as $\ln(1+z)$ to help show low and high redshift behavior simultaneously.

Any surprising result merits healthy skepticism, and the DESI findings are no exception. While the statistical significance is only moderate, it comes from measurement methods whose systematic uncertainties are thought to be small and well understood, and are quantified in the analysis. It is possible that either the BAO or CMB systematics have been underestimated, enough to reduce the preference for evolving dark energy to the level of a plausible statistical excursion. Notably, removing CMB lensing from the data vector reduces the reported statistical significance from 3.1σ to 2.7σ. Independent of DESI, the DES Collaboration reports a 3.2σ preference for $\mathtt{w_0w_a CDM}$ over ΛCDM using *Planck* CMB, DES SN, and the DES photometric BAO measurement [43]. There is a moderate "look elsewhere" effect in interpreting these numbers, as these studies could have found other forms of interesting departure from ΛCDM. However, the $w_0 - w_\mathrm{a}$ parameterization has been a standard component of dark energy analyses for many years, and the DESI and DES collaborations chose to consider this model before examining their data.

As shown in Figure 28.3, the distance ratio $D_\mathrm{M}(z \simeq 0.5)/D_\mathrm{M}(z \simeq 0.005)$ is a sharp discriminant

between the ΛCDM and $\mathtt{w_0w_a CDM}$ models. Supernovae are the most statistically powerful tool for measuring this ratio. Comparison of the DES and Pantheon+ results highlights the importance of calibrating local SNe relative to those at higher redshift. Here "calibration" encompasses not just the relative flux measurements, which are already challenging because of the large dynamic range, different observing facilities, and redshift-dependent mapping between observed and rest-frame wavelengths, but also the modeling of light-curve shape, intrinsic color variation, dust extinction, and sample biases (see, *e.g.*, [44]). Substantial efforts are underway to improve the calibration and the local SN samples (*e.g.*, [45, 46]). These studies may clarify whether SNe do or do not provide supporting evidence for evolving dark energy, and the samples of well observed SNe at $z > 0.1$ will grow dramatically with the advent of Rubin and *Roman*. Independent of SNe, the statistical precision of the DESI BAO measurements will improve by the end of the survey, and the AP effect at $z \simeq 2$ is another good discriminant between ΛCDM and $\mathtt{w_0w_a CDM}$. Ground-based CMB experiments are now providing independent tests of *Planck* results and somewhat greater statistical leverage on dark energy models. Stage IV weak lensing surveys should also reach the statistical precision needed to discriminate ΛCDM from the $\mathtt{w_0w_a CDM}$ model favored by DESI. Thus, if this model is correct, the statistical evidence for it should grow noticeably, and perhaps dramatically, over the next several years.

28.4.2 *The amplitude of matter clustering*

KiDS, DES, and HSC measure low redshift matter clustering (roughly $z < 1$) through cosmic shear and through "3×2 pt" analyses that combine cosmic shear with galaxy-shear and galaxy-galaxy correlation functions. These measurements provide constraints in the $(\sigma_8, \Omega_{\rm m})$ plane, often summarized in the parameter combination $S_8 \equiv \sigma_8(\Omega_{\rm m}/0.3)^{0.5}$. These analyses can be extended to include constraints from optical, X-ray, or SZ clusters, with mass profiles inferred from cluster-shear correlations. The growing precision and area of CMB lensing maps has made them a competitive tool for measuring galaxy-mass correlations without reliance on optical weak lensing data.

The amplitude of CMB anisotropies is proportional to the amplitude of density fluctuations present at recombination, and by assuming GR and a specified dark energy model one can extrapolate the growth of structure forward to the present day to predict σ_8. Many analyses find $(\sigma_8, \Omega_{\rm m})$ constraints that are consistent with *Planck*-normalized ΛCDM at the 1-2σ level, but most weak lensing measurements are at least somewhat below this prediction, some of them significantly so. For example, in the 2023 edition of this *Review*, we found that an average of weak lensing estimates of S_8 from different experiments gave a value 9.3% below the *Planck* prediction, with a significance of about 3σ if the statistical error was estimated from the dispersion among these six measurements.

The evidence for a discrepancy in S_8 looks weaker than it did two years ago, for several reasons. First, there has been an upward revision in the estimate of S_8 from cosmic shear in the final KiDS data set relative to earlier analyses [30], removing the previous tension with the *Planck*-normalized prediction. Reference [30] attributes this change primarily to improved calibration of photometric redshifts, though several factors may contribute. Second, there is increasing recognition that baryonic feedback effects might be large enough to suppress cosmic shear and galaxy-mass correlations out to scales included in current analyses. Third, the parameterization of intrinsic alignments adopted in many lensing analyses may be overly restrictive, leading to error estimates that are artificially small and correlated across experiments. The range of $(\sigma_8, \Omega_{\rm m})$ constraints from different experiments and analyses remains large, so it is premature to claim good agreement between CMB-normalized predictions and low-redshift measurements. However, there are promising routes for progress in the near future, including final results from DES and HSC, steadily improving measurements from CMB lensing, and RSD measurements from DESI, which should soon be statistically

competitive with weak lensing measurements. If GR is correct, then lensing-based measurements and RSD measurements should give consistent answers for σ_8 and $\Omega_{\rm m}$; in modified gravity models, the two measurements could give discrepant results because they respond to different combinations of gravitational potentials.

28.4.3 *The Hubble constant*

A flat ΛCDM model fit to *Planck* CMB data alone predicts $H_0 = (67.4 \pm 0.5)\ {\rm km\,s^{-1}\,Mpc^{-1}}$ (see Sec. 29 of this *Review*). This prediction and its error bar are sensitive to the assumptions of constant dark energy and a flat Universe. However, by adding BAO and supernova data one can construct an "inverse distance ladder" to measure H_0 precisely, even with a general dark energy model and free curvature [47]. Reference [36] applies this approach to obtain $H_0 = (68.2 \pm 0.81)\ {\rm km\,s^{-1}\,Mpc^{-1}}$, and other analyses combining CMB, BAO, and SN data give similar results. As discussed in Sec. 25.3.1 of this *Review*, some of the recent H_0 measurements from low-redshift data yield higher values. For example, Ref. [48] uses a distance ladder based on Cepheid calibration of Type Ia supernova luminosities to find $H_0 = (73.0 \pm 1.0)\ {\rm km\,s^{-1}\,Mpc^{-1}}$, in clear tension with cosmologically inferred values. New observations with the *James Webb Space Telescope* (*JWST*) allow Cepheid-based distance measurements with higher angular resolution and flux sensitivity, and their consistency with distances from *Hubble Space Telescope* is an important check on the robustness of these measurements [49]. However, some analyses based on tip-of-the-red-giant-branch (TRGB) or J-region asymptotic giant branch (JAGB) distance indicators give lower H_0 estimates consistent with the cosmological values [50].

The experimental situation with H_0 remains uncertain, though there are prospects for improvement with further *JWST* studies and *Gaia*-based parallaxes to more Galactic Cepheids. If the resolution lies in new physics rather than measurement errors, then this is probably physics that operates in the *pre-recombination* Universe, rescaling the BAO standard ruler in a way that shifts the ΛCDM and inverse-distance-ladder values upward. "Early dark energy" models can achieve this effect by increasing the early expansion rate, but these models must be finely tuned to satisfy constraints from the damping tail of CMB anisotropies and the shape of the galaxy power spectrum.

28.5 Summary and Outlook

The discovery of cosmic acceleration three decades ago came from a handful of expansion history and clustering measurements with roughly 10% precision, soon augmented by a more precise geometrical constraint from the CMB acoustic peak. Today's dark energy experiments have achieved $\sim 1\%$ measurements of the distance scale and expansion rate over a wide range of redshift ($0 \le z < 2.5$) and 2–5% measurements of matter clustering at $z < 1$. Contemporary CMB experiments also provide much more stringent constraints on the matter and baryon densities, the pre-recombination expansion history, and the amplitude and shape of the primordial power spectrum. At this higher level of precision and detail, the ΛCDM model is showing cracks. It is not clear which if any of those cracks are signs of new physics and which are signs of unrecognized or underestimated systematics.

Stage IV experiments hold the prospect of an order-of-magnitude gain in statistical power, and analyses that better exploit non-linear scales can sharpen constraints from existing and future data sets. Realizing these statistical gains requires comparable improvements in control of experimental and theoretical systematics. This is a challenging task, but large data sets allow new approaches to identifying and mitigating systematics, *e.g.*, by dividing source, lens, or supernova populations into subsets and testing for consistency, or by marginalizing over more flexible models of systematic effects. Stage IV surveys also offer substantial improvements in data quality, as well as data quantity.

If any of the currently suggested deviations from ΛCDM are real — 1–2% in the expansion

rate at $z \simeq 0.5$, 5–10% in H_0 or S_8 — then Stage IV experiments should be able to map these deviations in detail. For cosmological models that assume GR and minimally coupled dark energy, the observable effects are almost entirely captured by the expansion history $H(z)$, and different observational probes should yield consistent results for this governing function. However, the phenomenology could be much richer in models with modified gravity, or extensions to particle physics such as decaying dark matter or coupling between dark energy and other components. With a tightly constrained $H(z)$ from BAO+SN+CMB, weak lensing and RSD measurements can map the redshift, scale, and environment dependence of matter clustering, which could either reveal this rich phenomenology or set tight limits on departures from minimal GR-based models.

Of course, the tensions described in Section 28.4 may dissipate as the data and analysis methods improve. If so, the next generation of experiments could still reveal deviations from ΛCDM that are within the uncertainties of current data, though the detail with which these smaller deviations can be characterized will be more limited. Alternatively, ΛCDM could be the correct cosmological model, or so close that it is observationally indistinguishable, which would leave us with a relatively simple but frustratingly incomplete picture of dark energy and cosmic acceleration. We do not yet know which of these possibilities describes the Universe that we live in. We can hope that our experiments will reveal the cosmological equivalent of the anomalous precession of Mercury, and that discrepancies with our theoretical predictions will guide us to a new understanding of energy, or gravity, or the spacetime structure of the cosmos.

References

[1] A. Einstein, Sitzungsber. Preuss. Akad. Wiss. Berlin (Math. Phys.), 142 (1917).

[2] Ya. B. Zel'dovich, A. Krasinski and Ya. B. Zeldovich, Sov. Phys. Usp. **11**, 381 (1968), [Gen. Rel. Grav.40,1557(2008); Usp. Fiz. Nauk95,209(1968)].

[3] A. Friedman, Z. Phys. **10**, 377 (1922), [Gen. Rel. Grav.31,1991(1999)].

[4] G. Lemaître, Annales de la Societe Scietifique de Bruxelles **47**, 49 (1927).

[5] E. Hubble, Proc. Nat. Acad. Sci. **15**, 168 (1929).

[6] A. Einstein and W. de Sitter, Proc. Nat. Acad. Sci. **18**, 213 (1932).

[7] For background and definitions, see Big-Bang Cosmology – Sec. 22 of this *Review*.

[8] A. G. Riess *et al.* (Supernova Search Team), Astron. J. **116**, 1009 (1998), [arXiv:astro-ph/9805201].

[9] S. Perlmutter *et al.* (Supernova Cosmology Project), Astrophys. J. **517**, 565 (1999), [arXiv:astro-ph/9812133].

[10] P. de Bernardis *et al.* (Boomerang), Nature **404**, 955 (2000), [arXiv:astro-ph/0004404].

[11] S. Hanany *et al.*, Astrophys. J. **545**, L5 (2000), [arXiv:astro-ph/0005123].

[12] D. H. Weinberg *et al.*, Phys. Rept. **530**, 87 (2013), [arXiv:1201.2434].

[13] C. Wetterich, Nucl. Phys. **B302**, 668 (1988), [arXiv:1711.03844].

[14] A. Joyce *et al.*, Phys. Rept. **568**, 1 (2015), [arXiv:1407.0059].

[15] S. M. Carroll *et al.*, Phys. Rev. **D70**, 043528 (2004), [arXiv:astro-ph/0306438].

[16] G. R. Dvali, G. Gabadadze and M. Porrati, Phys. Lett. **B485**, 208 (2000), [hep-th/0005016].

[17] C.M. Will, Living Reviews in Relativity, **9**, 3 (2006). See also the chapter on Experimental Tests of Gravitational Theory — in this *Review*.

[18] J. Wang, L. Hui and J. Khoury, Phys. Rev. Lett. **109**, 241301 (2012), [arXiv:1208.4612].

[19] M. Fairbairn and A. Goobar, Phys. Lett. **B642**, 432 (2006), [arXiv:astro-ph/0511029]; Y.-S. Song, I. Sawicki and W. Hu, Phys. Rev. **D75**, 064003 (2007), [arXiv:astro-ph/0606286]; C. Blake *et al.*, Mon. Not. Roy. Astron. Soc. **415**, 2876 (2011), [arXiv:1104.2948].

[20] T. Baker *et al.*, Phys. Rev. Lett. **119**, 25, 251301 (2017), [arXiv:1710.06394].

[21] E. V. Linder, Phys. Rev. **D72**, 043529 (2005), [arXiv:astro-ph/0507263].

[22] This is essentially the FoM proposed in the Dark Energy Task Force (DETF) report, A. Albrecht *et al.*, `astro-ph/0609591,`though they based their FoM on the area of the 95% confidence contour in the $w_0 - w_a$ plane.

[23] T. Baker *et al.*, Rev. Mod. Phys. **93**, 1, 015003 (2021), [arXiv:1908.03430].

[24] For high accuracy, the impact of acoustic oscillations must be computed with a full Boltzmann code, but the simple integral for r_s captures the essential physics and the scaling with cosmological parameters.

[25] R. A. Sunyaev and Ya. B. Zeldovich, Astrophys. Space Sci. **7**, 3 (1970).

[26] D. Brout *et al.*, Astrophys. J. **938**, 2, 110 (2022), [arXiv:2202.04077].

[27] S.-F. Chen *et al.*, Mon. Not. Roy. Astron. Soc. **534**, 1, 544 (2024), [arXiv:2402.14070].

[28] C. Alcock and B. Paczynski, Nature **281**, 358 (1979).

[29] A. Albrecht *et al.* (2006), [arXiv:astro-ph/0609591].

[30] A. H. Wright *et al.* (2025), [arXiv:2503.19441].

[31] T. M. C. Abbott *et al.* (DES), Phys. Rev. D **105**, 2, 023520 (2022), [arXiv:2105.13549].

[32] R. Dalal *et al.*, Phys. Rev. D **108**, 12, 123519 (2023), [arXiv:2304.00701].

[33] D. Scolnic *et al.*, Astrophys. J. **938**, 2, 113 (2022), [arXiv:2112.03863].

[34] D. Rubin *et al.*, Astrophys. J. **986**, 2, 231 (2025), [arXiv:2311.12098].

[35] T. M. C. Abbott *et al.* (DES), Astrophys. J. Lett. **973**, 1, L14 (2024), [arXiv:2401.02929].

[36] S. Alam *et al.* (eBOSS), Phys. Rev. D **103**, 8, 083533 (2021), [arXiv:2007.08991].

[37] M. Abdul Karim *et al.* (DESI) (2025), [arXiv:2503.14738].

[38] J. C. Cuillandre *et al.* (Euclid), Astron. Astrophys. **697**, A6 (2025), [arXiv:2405.13496].

[39] Ž. Ivezić *et al.* (LSST), Astrophys. J. **873**, 2, 111 (2019), [arXiv:0805.2366].

[40] G. Zasowski *et al.* (2025), [arXiv:2505.10574].

[41] N. Aghanim *et al.* (Planck) (2018), [arXiv:1807.06209].

[42] W. Hu, Phys. Rev. D **71**, 047301 (2005), [arXiv:astro-ph/0410680].

[43] T. M. C. Abbott *et al.* (DES) (2025), [arXiv:2503.06712].

[44] M. Vincenzi *et al.* (DES) (2025), [arXiv:2501.06664].

[45] B. Popovic *et al.* (2025), [arXiv:2506.05471].

[46] M. Acevedo *et al.* (2025), [arXiv:2508.10877].

[47] E. Aubourg *et al.*, Phys. Rev. **D92**, 12, 123516 (2015), [arXiv:1411.1074].

[48] A. G. Riess *et al.*, Astrophys. J. Lett. **934**, 1, L7 (2022), [arXiv:2112.04510].

[49] A. G. Riess *et al.*, Astrophys. J. Lett. **962**, 1, L17 (2024), [arXiv:2401.04773].

[50] W. L. Freedman *et al.*, Astrophys. J. **985**, 2, 203 (2025), [arXiv:2408.06153].